Retrieving the displacement of strained nanoobjects: the impact of bounds for the scattering magnitude in direct space

Martin Köhl,* Philipp Schroth, A. A. Minkevich, and Tilo Baumbach

Institute for Photon Science and Synchrotron Radiation, Karlsruhe Institute of Technology, Hermann-von-Helmholtz-Platz 1, 76344 Eggenstein-Leopoldshafen, Germany

*martin.koehl@kit.edu

Abstract: Coherent X-ray diffraction imaging (CXDI) of the displacement field and strain distribution of nanostructures in kinematic far-field conditions requires solving a set of non-linear and non-local equations. One approach to solving these equations, which utilizes only the object's geometry and the intensity distribution in the vicinity of a Bragg peak as *a priori* knowledge, is the HIO+ER-algorithm. Despite its success for a number of applications, reconstruction in the case of highly strained nanostructures is likely to fail. To overcome the algorithm's current limitations, we propose the $\mathrm{HIO}^{\mathrm{M}}_{\mathrm{O_R}}$+$\mathrm{ER}^{\mathrm{M}}$-algorithm which allows taking advantage of additional *a priori* knowledge of the local scattering magnitude and remedies HIO+ER's stagnation by incorporation of randomized overrelaxation at the same time. This approach achieves significant improvements in CXDI data analysis at high strains and greatly reduces sensitivity to the reconstruction's initial guess. These benefits are demonstrated in a systematic numerical study for a periodic array of strained silicon nanowires. Finally, appropriate treatment of reciprocal space points below noise level is investigated.

OCIS codes: (100.5070) Phase retrieval; (100.3200) Inverse scattering; (100.3190) Inverse problems; (290.3200) Inverse scattering; (110.3200) Inverse scattering.

References and links

1. M. Köhl, A. A. Minkevich, and T. Baumbach, "Improved success rate and stability for phase retrieval by including randomized overrelaxation in the hybrid input output algorithm," Opt. Express **20**, 17093–17106 (2012).
2. J. A. Rodriguez, R. Xu, C.-C. Chen, Y. Zou, and J. Miao, "Oversampling smoothness: an effective algorithm for phase retrieval of noisy diffraction intensities," J. Appl. Crystallogr. **46**, 312–318 (2013).
3. D. E. Adams, L. S. Martin, M. D. Seaberg, D. F. Gardner, H. C. Kapteyn, and M. M. Murnane, "A generalization for optimized phase retrieval algorithms," Opt. Express **20**, 24778–24790 (2012).
4. A. A. Minkevich, T. Baumbach, M. Gailhanou, and O. Thomas, "Applicability of an iterative inversion algorithm to the diffraction patterns from inhomogeneously strained crystals," Phys. Rev. B **78**, 174110 (2008).
5. A. A. Minkevich, M. Gailhanou, J.-S. Micha, B. Charlet, V. Chamard, and O. Thomas, "Inversion of the diffraction pattern from an inhomogeneously strained crystal using an iterative algorithm," Phys. Rev. B **76**, 104106 (2007).
6. Y. Chushkin and F. Zontone, "Upsampling speckle patterns for coherent x-ray diffraction imaging," J. Appl. Crystallogr. **46**, 319–323 (2013).
7. R. Trahan and D. Hyland, "Mitigating the effect of noise in the hybrid input-output method of phase retrieval," Appl. Opt. **52**, 3031–3037 (2013).
8. G. Renaud, R. Lazzari, and F. Leroy, "Probing surface and interface morphology with grazing incidence small angle x-ray scattering," Surf. Sci. Rep. **64**, 255–380 (2009).
9. G. Binnig, C. F. Quate, and C. Gerber, "Atomic force microscope," Phys. Rev. Lett. **56**, 930–933 (1986).

#192722 - $15.00 USD Received 21 Jun 2013; revised 30 Aug 2013; accepted 2 Sep 2013; published 5 Nov 2013

10. F. J. Giessibl, "Advances in atomic force microscopy," Rev. Mod. Phys. **75**, 949–983 (2003).
11. S. Cuenot, C. Frétigny, S. Demoustier-Champagne, and B. Nysten, "Surface tension effect on the mechanical properties of nanomaterials measured by atomic force microscopy," Phys. Rev. B **69**, 165410 (2004).
12. N. Jalili and K. Laxminarayana, "A review of atomic force microscopy imaging systems: application to molecular metrology and biological sciences," Mechatronics **14**, 907 – 945 (2004).
13. L. Reimer, *Scanning Electron Microscopy: Physics of Image Formation and Microanalysis*, vol. 45 (Springer Series in Optical Sciences, 1998), 2nd ed.
14. A. Diaz, V. Chamard, C. Mocuta, R. Magalhães-Paniago, J. Stangl, D. Carbone, T. H. Metzger, and G. Bauer, "Imaging the displacement field within epitaxial nanostructures by coherent diffraction: a feasibility study," New J. Phys. **12**, 035006 (2010).
15. S. T. Haag, M.-I. Richard, S. Labat, M. Gailhanou, U. Welzel, E. J. Mittemeijer, and O. Thomas, "Anomalous coherent diffraction of core-shell nano-objects: a methodology for determination of composition and strain fields," Phys. Rev. B **87**, 035408 (2013).
16. P. Godard, G. Carbone, M. Allain, F. Mastropietro, G. Chen, L. Capello, A. Diaz, T. Metzger, J. Stangl, and V. Chamard, "Three-dimensional high-resolution quantitative microscopy of extended crystals," Nat. Commun. **2**, 568 (2011).
17. M. Dierolf, A. Menzel, P. Thibault, P. Schneider, C. Kewish, R. Wepf, O. Bunk, and F. Pfeiffer, "Ptychographic x-ray computed tomography at the nanoscale," Nature **467**, 436 (2010).
18. I. Robinson and R. Harder, "Coherent x-ray diffraction imaging of strain at the nanoscale," Nat. Mater. **8**, 291–298 (2009).
19. Y. Nishino, Y. Takahashi, N. Imamoto, T. Ishikawa, and K. Maeshima, "Three-dimensional visualization of a human chromosome using coherent x-ray diffraction," Phys. Rev. Lett. **102**, 018101 (2009).
20. C. G. Schroer, P. Boye, J. M. Feldkamp, J. Patommel, A. Schropp, A. Schwab, S. Stephan, M. Burghammer, S. Schöder, and C. Riekel, "Coherent x-ray diffraction imaging with nanofocused illumination," Phys. Rev. Lett. **101**, 090801 (2008).
21. J. Miao, P. Charalambous, J. Kirz, and D. Sayre, "Extending the methodology of x-ray crystallography to allow imaging of micrometre-sized non-crystalline specimens," Nature **400**, 342–344 (1999).
22. M. A. Pfeifer, G. J. Williams, I. A. Vartanyants, R. Harder, and I. K. Robinson, "Three-dimensional mapping of a deformation field inside a nanocrystal," Nature **442**, 63–66 (2006).
23. A. Biermanns, A. Davydok, H. Paetzelt, A. Diaz, V. Gottschalch, T. H. Metzger, and U. Pietsch, "Individual GaAs nanorods imaged by coherent x-ray diffraction," J. Synchrotron Radiat. **16**, 796–802 (2009).
24. A. A. Minkevich, E. Fohtung, T. Slobodskyy, M. Riotte, D. Grigoriev, T. Metzger, A. C. Irvine, V. Novák, V. Holý, and T. Baumbach, "Strain field in (Ga,Mn)As/GaAs periodic wires revealed by coherent x-ray diffraction," Europhys. Lett. **94**, 66001 (2011).
25. A. A. Minkevich, E. Fohtung, T. Slobodskyy, M. Riotte, D. Grigoriev, M. Schmidbauer, A. C. Irvine, V. Novák, V. Holý, and T. Baumbach, "Selective coherent x-ray diffractive imaging of displacement fields in (Ga,Mn)As/GaAs periodic wires," Phys. Rev. B **84**, 054113 (2011).
26. R. Millane, "Phase retrieval in crystallography and optics," J. Opt. Soc. Am. A **7**, 394–411 (1990).
27. S. G. Podorov, K. M. Pavlov, and D. M. Paganin, "A non-iterative reconstruction method for direct and unambiguous coherent diffractive imaging," Opt. Express **15**, 9954–9962 (2007).
28. I. A. Vartanyants and I. K. Robinson, "Partial coherence effects on the imaging of small crystals using coherent x-ray diffraction," J. Phys.: Condens. Matter **13**, 10593–10611 (2001).
29. J. Fienup, "Phase retrieval algorithms: a comparison," Appl. Opt. **21**, 2758–2769 (1982).
30. J. Fienup, "Reconstruction of a complex-valued object from the modulus of its Fourier transform using a support constraint," J. Opt. Soc. Am. A **4**, 118–123 (1986).
31. S. Marchesini, "A unified evaluation of iterative projection algorithms for phase retrieval," Rev. Sci. Instrum. **78**, 011301 (2007).
32. S. Marchesini, "Phase retrieval and saddle-point optimization," J. Opt. Soc. Am. A **24**, 3289–3296 (2007).
33. A. Levi and H. Stark, "Image restoration by the method of generalized projections with application to restoration from magnitude," J. Opt. Soc. Am. A **1**, 932–943 (1984).
34. D. C. Youla and H. Webb, "Image restoration by the method of convex projections: part 1 - theory," IEEE Trans. Med. Imaging **1**, 81–94 (1982).
35. K. Busch, G. von Freymann, S. Linden, S. F. Mingaleev, L. Tkeshelashvili, and M. Wegener, "Periodic nanostructures for photonics," Phys. Rep. **444**, 101 (2007).
36. K. Busch, C. Blum, A. M. Graham, D. Hermann, M. Köhl, P. Mack, and C. Wolff, "The photonic Wannier function approach to photonic crystal simulations: status and perspectives," J. Mod. Opt. **58**, 365–383 (2011).
37. M. Köhl, C. Wolff, and K. Busch, "Cluster coherent potential approximation for disordered photonic crystals using photonic Wannier functions," Opt. Lett. **37**, 560–562 (2012).
38. K. Busch, S. F. Mingaleev, A. Garcia-Martin, M. Schillinger, and D. Hermann, "The Wannier function approach to photonic crystal circuits," J. Phys. Condens. Matter **15**, R1233 (2003).
39. S. John, "Strong localization of photons in certain disordered dielectric superlattices," Phys. Rev. Lett. **58**, 2486–2489 (1987).

#192722 - $15.00 USD Received 21 Jun 2013; revised 30 Aug 2013; accepted 2 Sep 2013; published 5 Nov 2013

40. E. Yablonovitch, "Inhibited spontaneous emission in solid-state physics and electronics," Phys. Rev. Lett. **58**, 2059–2062 (1987).
41. S. Takagi, "A dynamical theory of diffraction for a distorted crystal," J. Phys. Soc. Jpn. **26**, 1239–1253 (1969).
42. U. Pietsch, V. Holy, and T. Baumbach, *High-Resolution X-Ray Scattering from Thin Films to Lateral Nanostructures* (Springer, New York, 2004).
43. J.-F. Weng and Y.-L. Lo, "Novel rotation algorithm for phase unwrapping applications," Opt. Express **20**, 16838–16860 (2012).
44. T. Benabbas, Y. Androussi, and A. Lefebvre, "A finite-element study of strain fields in vertically aligned InAs islands in GaAs," J. Appl. Phys. **86**, 1945–1950 (1999).
45. M. Hanke, D. Grigoriev, M. Schmidbauer, P. Schäfer, R. Köhler, U. Pohl, R. Sellin, D. Bimberg, N. Zakharov, and P. Werner, "Diffuse x-ray scattering of InGaAs/GaAs quantum dots," Physica E **21**, 684 – 688 (2004). Proceedings of the Eleventh International Conference on Modulated Semiconductor Structures.
46. M. Hanke, D. Grigoriev, M. Schmidbauer, P. Schäfer, R. Köhler, R. L. Sellin, U. W. Pohl, and D. Bimberg, "Vertical composition gradient in InGaAs/GaAs alloy quantum dots as revealed by high-resolution x-ray diffraction," Appl. Phys. Lett. **85**, 3062 (2004).
47. G. R. Liu and S. S. Q. Jerry, "A finite element study of the stress and strain fields of InAs quantum dots embedded in GaAs," Semicond. Sci. Technol. **17**, 630–643 (2002).
48. M. Hanke, Y. I. Mazur, J. E. Marega, Z. Y. AbuWaar, G. J. Salamo, P. Schäfer, and M. Schmidbauer, "Shape transformation during overgrowth of InGaAs/GaAs(001) quantum rings," Appl. Phys. Lett. **91**, 043103 (2007).
49. P. Schroth, T. Slobodskyy, D. Grigoriev, A. Minkevich, M. Riotte, S. Lazarev, E. Fohtung, D. Hu, D. Schaadt, and T. Baumbach, "Investigation of buried quantum dots using grazing incidence x-ray diffraction," Mater. Sci. Eng., B **177**, 721–724 (2012).
50. M. Eberlein, S. Escoubas, M. Gailhanou, O. Thomas, J.-S. Micha, P. Rohr, and R. Coppard, "Investigation by high resolution x-ray diffraction of the local strains induced in Si by periodic arrays of oxide filled trenches," Phys. Status Solidi A **204**, 2542–2547 (2007).
51. M. Eberlein, S. Escoubas, M. Gailhanou, O. Thomas, P. Rohr, and R. Coppard, "Influence of crystallographic orientation on local strains in silicon: a combined high-resolution x-ray diffraction and finite element modelling investigation," Thin Solid Films **516**, 8042–8048 (2008).
52. P. Thibault, V. Elser, C. Jacobsen, D. Shapiro, and D. Sayre, "Reconstruction of a yeast cell from x-ray diffraction data," Acta Crystallogr., Sect. A: Found. Crystallogr. **62**, 248–261 (2006).
53. M. Frigo and S. Johnson, "The design and implementation of FFTW3," Proc. IEEE **93**, 216–231 (Feb.).
54. R. P. Millane, "Multidimensional phase problems," J. Opt. Soc. Am. A **13**, 725–734 (1996).
55. J. H. Seldin and J. R. Fienup, "Numerical investigation of the uniqueness of phase retrieval," J. Opt. Soc. Am. A **7**, 412–427 (1990).
56. R. H. T. Bates, "Fourier phase problems are uniquely solvable in more than one dimension," Optik (Stuttgart) **61**, 247–262 (1982).

Coherent X-ray diffraction imaging (CXDI) has great potential for investigating the displacement field of inhomogeneously strained nanostructures in a non-destructive manner. Such investigations typically focus on the coherently scattered intensity distribution $\mathbf{I}_{Q_\mathrm{B}}(q)$ in the vicinity of one or more Bragg peaks Q_B, which is determined by the displacement field u, the shape Ω of the nanocrystal and its chemical composition profile within a specific framework of approximations. q denotes the distance in reciprocal space from the Bragg peak Q_B.

Given far field conditions, the intensity $\mathbf{I}_{Q_\mathrm{B}}(q)$ is proportional to $|\mathfrak{f}(Q_\mathrm{B}+q)|^2 = |\mathbf{FT}_{Q_\mathrm{B}+q\leftarrow x}\{\rho_\mathrm{el}(x)\}|^2$ where $\rho_\mathrm{el}(x)$ is the electron density of the illuminated sample. However, a measurement of the intensity distribution $\mathbf{I}_{Q_\mathrm{B}}(q)$ does not reveal the q-dependence of the phase information $\arg(\mathfrak{f}(Q_\mathrm{B}+q))$. Once this phase information is available, the displacement field u is obtained by inverse Fourier transform. Consequently, considerable efforts are put in the development of robust algorithms for retrieving this lost phase information based on proper *a priori* knowledge [1–7].

One recent technique aiming to extract the nanostructure's displacement field u from the coherently scattered intensity $\mathbf{I}_{Q_\mathrm{B}}(q)$ utilizes the object's geometry Ω as *a priori* knowledge combined with proper reconstruction algorithms. The shape Ω can be accessed by complementary techniques like GISAXS [8], AFM [9–12] or SEM [13]. By this approach, several inhomogeneously strained nano-sized objects like quantum dots and quantum wires have already been inspected at synchrotron facilities by CXDI [2, 5, 6, 14–28]. In most cases, a combination

#192722 - $15.00 USD Received 21 Jun 2013; revised 30 Aug 2013; accepted 2 Sep 2013; published 5 Nov 2013

of the hybrid input output algorithm (HIO-algorithm) and error reduction (ER-algorithm) has been employed [29–31] to solve the non-linear non-local system of equations underlying the reconstruction of the displacement field. Despite great success of this algorithm for a number of applications, its capabilities are not yet fully satisfactory [1, 2, 31]. The frequent failure of the method for highly inhomogeneously strained systems forced researchers to explore novel strategies to overcome current limitations. For this purpose, mainly two strategies are pursued:

On the one hand, the incorporation of additional *a priori* knowledge in direct space beyond the object's geometry proved valuable for retrieving the displacement field u from a particular experimental data set of a highly inhomogeneously strained nanostructure [2, 4, 5]. However, additional *a priori* knowledge does not eliminate the non-convex operations involved during reconstruction. These operations are claimed to cause stagnation or convergence to local minima and typically imply a strong dependence on the initial guess of the reconstruction.

On the other hand, novel algorithms which do not require additional *a priori* knowledge in comparison to the existing algorithms are developed [1, 3, 7, 31, 32]. One such algorithm is the $\mathrm{HIO}_{\mathrm{O_R}}$+ER-algorithm [1]: it is an extension of the HIO+ER-algorithm [29, 30] based on randomized overrelaxation [33, 34]. This way some residual shortcomings [1, 31] of the traditional HIO+ER-algorithm could be overcome without requiring additional *a priori* knowledge beyond shape Ω in direct space and intensity distribution $\mathbf{I}_{Q_\mathrm{B}}(q)$ in reciprocal space. In particular, the dependence on the initial guess of the reconstruction is reduced significantly. Therefore, the combination of randomized overrelaxation and additional *a priori* knowledge is very promising.

In the present manuscript a systematic numerical study of a periodic array of strained silicon nanowires reveals current capabilities and limitations of CXDI data analysis: For the first time, the interplay of randomized overrelaxation (in reciprocal space) and additional *a priori*-knowledge in direct space is studied. In the authors' opinion, the most relevant direct space constraints are lower and upper bounds on the local scattering magnitude and, therefore, have been chosen for this investigation.

The structure of the manuscript is as follows: In Sec. 1, we discuss the theoretical background of our investigation: First, we review the system of equations which CXDI reconstruction algorithms need to solve. Then, we define and discuss the constraints on the local scattering magnitude and their incorporation in the $\mathrm{HIO}_{\mathrm{O_R}}$+ER-algorithm. We refer to the resulting algorithm as $\mathrm{HIO}^{\mathrm{M}}_{\mathrm{O_R}}$+$\mathrm{ER}^{\mathrm{M}}$-algorithm. Next, we introduce the physical system we have chosen for our investigation — a periodic array of strained silicon nanowires. The next subsection in the theoretical background is devoted to the figure of merits which are important for judging the output of the reconstruction procedure. Finally, we introduce models for treating (the typically large fraction of) reciprocal space data points which are so weak that the true signal is superseded by noise in experimental data. In Sec. 2, we apply the $\mathrm{HIO}^{\mathrm{M}}_{\mathrm{O_R}}$+$\mathrm{ER}^{\mathrm{M}}$-algorithm to our physical model system and systematically increase the strain until the reconstruction process fails. First, ideal data is considered. Finally, the behavior for missing low signal information within the concepts introduced in Sec. 1.4 is investigated in Sec. 2.2.

Our results demonstrate that the $\mathrm{HIO}^{\mathrm{M}}_{\mathrm{O_R}}$+$\mathrm{ER}^{\mathrm{M}}$-algorithm constitutes a major improvement for the investigation of inhomogeneously strained nanocrystals in comparison to the traditional HIO+ER-algorithm.

1. Theoretical background

This section summarizes the theoretical basis underlying current phase retrieval techniques which aim to extract the displacement field of inhomogeneously strained nanocrystals.

We restrict to phase retrieval techniques based on kinematic theory and far-field limit. Absorption is neglected. The coherence volume of the impinging beam is assumed to be bigger

#192722 - $15.00 USD Received 21 Jun 2013; revised 30 Aug 2013; accepted 2 Sep 2013; published 5 Nov 2013

than the sample's strained region. Our discussion does not include multiple scattering which is negligible as long as the extension of the sample domain under investigation is much smaller than the mean free path of the propagating radiation. Whereas this length decreases for "typical" photonic crystals illuminated at optical frequencies to a single (photonic) unit cell [35–40], coherent X-ray radiation is suited for the investigation of nanocrystalline samples containing a huge number of (atomic) unit cells.

These approximations relate the scattering factor

$$\mathfrak{f}(Q) = \mathbf{FT}_{Q \leftarrow x}\{\rho_{\mathrm{el}}(x)\} = \int_{\mathbb{R}^d} \mathrm{d}^d x \, \rho_{\mathrm{el}}(x) \mathrm{e}^{\mathrm{i}Q\cdot x} \tag{1}$$

of the nanostructure to the experimentally measured intensity distribution $\mathbf{I}(q)$ of the scattered incident radiation by $\mathbf{I}(Q) \propto |\mathfrak{f}(Q)|^2$ where $Q = k_{\mathrm{Out}} - k_{\mathrm{In}}$ is the scattering vector. k_{In} and k_{Out} are the incident and outgoing wave vector respectively. $\rho_{\mathrm{el}}(x)$ is the electron density of the nanostructure. We restrict to the displacement in samples which can be considered as inhomogeneously strained crystalline structures with fully elastic strain. Heterogeneous material systems are included as long as their interface is coupled elastically. In the vicinity of a Bragg peak $Q_{\mathrm{B}} \neq \vec{0}$, the contribution of amorphous domains in the sample to the scattered intensity is typically negligible. So, amorphous domains may also be present in the nanostructure.

The (by assumption coherently scattered) intensity $\mathbf{I}_{Q_{\mathrm{B}}}(q)$, where $q = k_{\mathrm{Out}} - k_{\mathrm{In}} - Q_{\mathrm{B}}$ denotes the distance from the scattering vector Q to the Bragg peak Q_{B}, can be simplified further in a Bragg peak's vicinity for $Q_{\mathrm{B}} \neq \vec{0}$: It is valid to substitute the full electron density $\rho_{\mathrm{el}}(x)$ in Eq. (1) by the complex valued effective electron density

$$\rho_{\mathrm{eff}}(x, Q_{\mathrm{B}}) \equiv \mathrm{e}^{\mathrm{i}Q_{\mathrm{B}}\cdot u(x)} \zeta_{Q_{\mathrm{B}}}(x) \Omega(x) \equiv \mathbf{IFT}_{x \leftarrow q}\{\mathfrak{f}_{Q_{\mathrm{B}}}(q)\} \, . \tag{2}$$

In this equation, $\Omega(x)$ describes the geometry of the strained crystalline region of the sample under consideration. Its value is one for any point x inside this strained region and zero otherwise. In the framework of the Takagi approximation [41, 42] for chemically homogeneous samples, the local scattering magnitude $\zeta_{Q_{\mathrm{B}}}(x)$ is a constant complex number. If we allow small changes in the chemical composition of the sample, $\zeta_{Q_{\mathrm{B}}}(x)$ varies in phase and amplitude, but its phase variation is typically much smaller than the contribution from $Q_{\mathrm{B}} \cdot u(x)$. Therefore, we neglect the phase contribution $\arg\left(\zeta_{Q_{\mathrm{B}}}(x)\right)$. Thus, $\zeta_{Q_{\mathrm{B}}}(x)$ reduces to a complex function with constant phase, but a small variation in magnitude related to the local chemical composition. This constant phase of $\zeta_{Q_{\mathrm{B}}}(x)$ is physically irrelevant. As a consequence, $\zeta_{Q_{\mathrm{B}}}(x)$ can be considered a real function of almost constant magnitude. Hence,

$$\mathbf{I}_{Q_{\mathrm{B}}}(q) \propto \left|\mathfrak{f}_{Q_{\mathrm{B}}}(q)\right|^2 = \left|\mathbf{FT}_{q \leftarrow x}\{\rho_{\mathrm{eff}}(x)\}\right|^2 \, . \tag{3}$$

The remainder of this manuscript is based upon the model (2) combined with Eq. (3) and will focus on finding the solution $\rho_{\mathrm{eff}}(x)$ given either only the shape $\Omega(x)$ and the amplitudes $\Gamma_q = \sqrt{\mathbf{I}_{Q_{\mathrm{B}}}(q)}$ or given this information plus additional knowledge of $\zeta_{Q_{\mathrm{B}}}(x)$. If this additional knowledge is exploited in the reconstruction procedure, the range of applicability of phase retrieval is significantly extended to higher values of strain and the robustness of the method for equal strain distribution is increased. Some remarks on uniqueness of the solution and numerical discretization can be found in Sec. A in the appendix.

1.1. The HIO$^{\mathrm{M}}_{O_R}$+ER$^{\mathrm{M}}$-algorithm

In this section, we extend the $\mathrm{HIO}_{\mathrm{O_R}}$+ER-algorithm [1, 29] to additionally incorporate lower and upper bounds on the local scattering magnitude $\zeta_{Q_{\mathrm{B}}}$. The $\mathrm{HIO}_{\mathrm{O_R}}$+ER-algorithm is an iterative procedure which is build up by two blocks, $\mathrm{HIO}_{\mathrm{O_R}}$ and ER. Each iteration of the

#192722 - $15.00 USD Received 21 Jun 2013; revised 30 Aug 2013; accepted 2 Sep 2013; published 5 Nov 2013

$\mathrm{HIO}_{\mathrm{O_R}}$+ER-algorithm N_{HIO} repetitions of the $\mathrm{HIO}_{\mathrm{O_R}}$-algorithm are performed, followed by N_{ER} repetitions of the ER-algorithm. We shortly summarize both building blocks:

The ER-algorithm [29, 30] is defined by

$$\mathfrak{f}_{Q_{\mathrm{B}}}^{(i+1)} = \hat{H}_{\mathrm{ER}}\, \mathfrak{f}_{Q_{\mathrm{B}}}^{(i)}\ ,\ \hat{H}_{\mathrm{ER}} = (\mathbf{FT})\ \mathbf{P}_{\Omega}\ (\mathbf{IFT})\ \mathbf{P}_{\Gamma}\ . \tag{4}$$

$\mathbf{P}_{\Omega}$ is a linear projection operator on the interior of the object's geometry Ω, i.e.,

$$\mathbf{P}_{\Omega}\ \rho_{\mathrm{eff}}^{(i)}(x) = \begin{cases} \rho_{\mathrm{eff}}^{(i)}(x) & \text{if } x \in \Omega\ , \\ 0 & \text{if } x \notin \Omega\ . \end{cases} \tag{5}$$

$\mathbf{P}_{\Gamma}$ is a non-linear and non-convex projection operator in reciprocal space. It enforces the amplitudes Γ_q in $\mathfrak{f}^{(i)}(q)$ without modifying the phases $\arg\left(\mathfrak{f}^{(i)}(q)\right)$. Hence, its formal definition is

$$\mathbf{P}_{\Gamma}\ \mathfrak{f}^{(i)}(q) = \Gamma_q\ \mathrm{e}^{\mathrm{i}\ \arg\left(\mathfrak{f}^{(i)}(q)\right)}\ . \tag{6}$$

The $\mathrm{HIO}_{\mathrm{O_R}}$-algorithm can be interpreted as a feedback based iterative mapping with feedback parameter β. A single iterative step is defined as

$$\rho_{\mathrm{eff}}^{(i+1)}(x) = \begin{cases} \mathbf{M}_{\mathrm{C}}(\lambda_{\Gamma})\,\rho_{\mathrm{eff}}^{(i)}(x) & \text{if } x \in \Omega\ , \\ \rho_{\mathrm{eff}}^{(i)}(x) - \beta \mathbf{M}_{\mathrm{C}}(\lambda_{\Gamma})\,\rho_{\mathrm{eff}}^{(i)}(x) & \text{if } x \notin \Omega\ , \end{cases} \tag{7a}$$

where the mapping

$$\mathbf{M}_{\mathrm{C}}(\lambda_{\Gamma}) = (\mathbf{IFT})\ \mathbf{Q}_{\Gamma;\lambda_{\Gamma}}(\mathbf{FT})\ . \tag{7b}$$

incorporates all available constraints and information except finite direct space geometry Ω. $\mathbf{Q}_{\Gamma;\lambda_{\Gamma}}$ is the overrelaxed map of $\mathbf{P}_{\Gamma}$, i.e.,

$$\mathbf{Q}_{\Gamma;\lambda_{\Gamma}} = 1 + \lambda_{\Gamma}\,(\mathbf{P}_{\Gamma} - 1)\ . \tag{7c}$$

Whereas overrelaxation with a *fixed* relaxation parameter λ_{Γ} typically even decreases the performance of the HIO-algorithm, randomization of the relaxation parameter turned out to be a key feature for overcoming stagnation in the iterative procedure [1]. Each iteration, the overrelaxation parameter λ_{Γ} is drawn from a uniform random distribution in the interval $[1-\nu, 1+\nu]$, $\nu \geq 0$. Unless stated otherwise, we choose $\nu = 0.5$. The success of the $\mathrm{HIO}_{\mathrm{O_R}}$+ER-algorithm neither depends sensitively on the value of parameter β in the range $[0.5, 1.0]$ nor on the particular choice of the internal parameters N_{HIO} and N_{ER} for $\nu \approx 0.5$ [1]. The traditional HIO+ER-algorithm is contained for $\nu = 0$ (i.e., $\lambda_{\Gamma} \equiv 1$).

Finally, we need to specify the initial guess of the iterative procedure. We choose

$$\mathfrak{f}_{Q_{\mathrm{B}}}^{(0)}(q) = \Gamma_q\, \mathrm{e}^{\mathrm{i}\Phi_q} \tag{8}$$

with randomly generated phases Φ_q at each point q.

Once a solution for $\mathfrak{f}(q)$ is found (and, therefore, the solution for $\rho_{\mathrm{eff}}(x)$), we can rely on Eq. (2) to extract the displacement field u. Depending on the amount of strain in the sample and the value of Q_{B}, unwrapping [43] of the phase (not considered in this manuscript) may or may not be necessary.

Incorporation of additional *a priori* knowledge may significantly expand the range of applicability of CXDI to highly inhomogeneously strained samples [4, 5]. Therefore, we now focus on incorporating assumptions on the local scattering magnitude $\zeta(x)$ (see Eq. (2)) in the $\mathrm{HIO}_{\mathrm{O_R}}$+ER-algorithm. The following property is true for most experimental samples: We can define sample domains $\Omega_j \subseteq \Omega$ in which the local scattering magnitude $\zeta(x)$ deviates only

#192722 - $15.00 USD Received 21 Jun 2013; revised 30 Aug 2013; accepted 2 Sep 2013; published 5 Nov 2013

slightly from its average value (e.g., substrate region or full sample in case of homogeneous chemical composition). The unification of the domains Ω_j does not need to coincide with the full sample Ω. Moreover, the domains may even overlap.

The most stringent case for this assumption is a chemically homogeneous material, for which the scattering magnitude $\zeta(x)$ is constant as long as we neglect the changes originating in strain. Hence, the deviation of $\zeta(x)$ from its average is equal to zero. If the nanostructure is not fully chemically homogeneous, at least the substrate region can typically be considered chemically homogeneous and almost unstrained. Hence, the scattering magnitude in this subdomain of the full structure deviates only slightly from this subdomain's average value – independent of the local scattering magnitude of additionally grown nanostructures on top. For the nanostructure on top of the substrate, we can constrain $\zeta(x)$ in addition with bounds representing a different average and a larger distance to this average.

For the remainder of this manuscript, we focus on this kind of direct space constraints and turn to the question of their proper implementation: limiting $\zeta(x)$ by

$$\mathrm{M_{L,j}}\bar{\zeta}_j \leq \zeta(x) \leq \mathrm{M_{H,j}}\bar{\zeta}_j \;\forall\, x \in \Omega_j \subseteq \Omega\;, \tag{9}$$

where Ω_j are the domains to be constrained. $\mathrm{M_{L,j}} \leq 1$ and $\mathrm{M_{H,j}} \geq 1$ are additional parameters which need to be known *a priori* for every domain j. Moreover, the lower and upper bounds $\mathrm{M_{L,j}}$ and $\mathrm{M_{H,j}}$ fulfill $\mathrm{M_{H,m}}\bar{\zeta}_m \geq \mathrm{M_{L,n}}\bar{\zeta}_n$ and $\mathrm{M_{L,m}}\bar{\zeta}_m \leq \mathrm{M_{H,n}}\bar{\zeta}_n$, if the domains Ω_m and Ω_n intersect.

We now define the set of (nonlinear) operators

$$\mathbf{M}_{\mathrm{M}}^{(j)}\,\rho_{\mathrm{eff}}^{(i)}(x) = \begin{cases} \mathrm{M}_j^{(i)}(x)\;\mathrm{e}^{\,\mathrm{i}\,\arg\left(\rho_{\mathrm{eff}}^{(i)}(x)\right)} & \text{if } x \in \Omega_j\;, \\ \rho_{\mathrm{eff}}^{(i)}(x) & \text{if } x \notin \Omega_j\;, \end{cases} \tag{10a}$$

$$\mathrm{M}_j^{(i)}(x) = \min\left(\mathrm{M_{H,j}}\bar{\zeta}_j^{(i)}; \max\left(\mathrm{M_{L,j}}\bar{\zeta}_j^{(i)}; \left|\rho_{\mathrm{eff}}^{(i)}(x)\right|\right)\right)\;, \tag{10b}$$

where (i) labels iterations and (j) labels the domains Ω_j. Each iteration, the averages $\bar{\zeta}_j$ are estimated during reconstruction by evaluating

$$\bar{\zeta}_j^{(i)} = \sqrt{\left\langle \mathbf{P}_{\Omega_j}\left|\rho_{\mathrm{eff}}^{(i)}\right|\,;\mathbf{P}_{\Omega_j}\left|\rho_{\mathrm{eff}}^{(i)}\right|\right\rangle / \left\langle \mathbf{P}_{\Omega_j};\mathbf{P}_{\Omega_j}\right\rangle}\,. \tag{10c}$$

Note, that in general the mappings $\mathbf{M}_{\mathrm{M}}^{(j)}$ are no projection operators: If one of them is applied repeatedly to an object, the average during the next action may be different from the current one. Thus, the operator is no longer idempotent as required for a projection operator. An exception is the case $\mathrm{M_{L,j}} = \mathrm{M_{H,j}} = 1$. In this case, applying a mapping $\mathbf{M}_{\mathrm{M}}^{(j)}$ repeatedly yields in the same result as applying it once.

The constraints $\mathbf{M}_{\mathrm{M}}^{(j)}$ can be incorporated in the $\mathrm{HIO_{O_R}}$+ER-algorithm by modifying $\mathbf{M}_{\mathrm{C}}(\lambda_\Gamma)$ (see Eq. (7b)) to

$$\mathbf{M}_{\mathrm{C}}(\lambda_\Gamma) = \mathbf{M}_{\mathrm{M}}\;(\mathbf{IFT})\;\mathbf{Q}_{\Gamma;\lambda_\Gamma}\;(\mathbf{FT})\;,\; \mathbf{M}_{\mathrm{M}} = \prod_j \mathbf{M}_{\mathrm{M}}^{(j)}\;. \tag{11}$$

At this point, we define the $\mathrm{HIO}_{\mathrm{O_R}}^{\mathrm{M}}$-algorithm by Eqs. (7a) and (11) (see Fig. 1). The solution $\rho_{\mathrm{eff}}(x)$ remains a fixed point of the iterative procedure for the proposed extension (11) due to the fact that $\mathbf{M}_{\mathrm{C}}$ reduces to $\mathbf{M}_{\mathrm{C}} \equiv 1$ if applied to $\rho_{\mathrm{eff}}(x)$. For the ER^{M}-algorithm, we employ

$$\hat{H}_{\mathrm{ER,M}}^{(\mathrm{OP})} = (\mathbf{FT})\;\mathbf{P}_\Omega\;\mathbf{M}_{\mathrm{M}}\;(\mathbf{IFT})\;\mathbf{P}_\Gamma \tag{12}$$

#192722 - $15.00 USD Received 21 Jun 2013; revised 30 Aug 2013; accepted 2 Sep 2013; published 5 Nov 2013

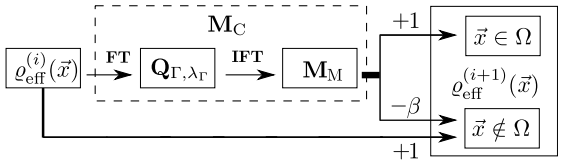

Fig. 1. Schematics of the $\mathrm{HIO}^{\mathrm{M}}_{\mathrm{O_R}}$-algorithm according to Eqs. (7a) and (11): In addition to $\mathbf{Q}_{\Gamma;\lambda_\Gamma}$ in the $\mathrm{HIO}_{\mathrm{O_R}}$-algorithm the operator $\mathbf{M}_\mathrm{M}$ is applied before the calculation of the next iterative candidate $\rho_\mathrm{eff}^{(i+1)}(x)$ is performed. In the limit $\mathrm{M_{L,n}} \to 0$ and $\mathrm{M_{H,n}} \to \infty$ for all n, the algorithm reduces to $\mathrm{HIO}_{\mathrm{O_R}}$ because $\mathbf{M}_\mathrm{M} \to 1$.

instead of Eq. (4). Finally, we define the $\mathrm{HIO}^{\mathrm{M}}_{\mathrm{O_R}}$+$\mathrm{ER}^{\mathrm{M}}$-algorithm as a combiniation of N_HIO iterations of $\mathrm{HIO}^{\mathrm{M}}_{\mathrm{O_R}}$-algorithm followed by N_ER iterations of the ER^{M}-algorithm. The $\mathrm{HIO}^{\mathrm{M}}_{\mathrm{O_R}}$+$\mathrm{ER}^{\mathrm{M}}$-algorithm is computational as efficient as $\mathrm{HIO}_{\mathrm{O_R}}$+ER and standard HIO+ER: All extensions can be implemented numerically as local, independent single pixel operations. Thus, they can be performed very efficiently and executed in parallel. Hence, computational efficiency is limited by the $N\log(N)$-scaling of the FFT algorithm.

At this point we want to stress the different nature of both modifications of $\mathrm{HIO}^{\mathrm{M}}_{\mathrm{O_R}}$+$\mathrm{ER}^{\mathrm{M}}$ with respect to standard HIO+ER: Whereas randomized overrelaxation tries to exploit the *same* set of given *a priori* knowledge — either $\{\Omega(x), \Gamma_q\}$ or $\{\Omega(x), \Gamma_q, \mathrm{M_{L,}}(x), \mathrm{M_{H,}}(x)\}$ in our case — more successfully, the constraints $\mathbf{M}_\mathrm{M}$ aim at regularization of the model (2) by adding the *additional a priori* knowledge $\{\mathrm{M_{L,}}(x), \mathrm{M_{H,}}(x)\}$.

1.2. Generation of the input data for the reconstruction

The benefits of the $\mathrm{HIO}^{\mathrm{M}}_{\mathrm{O_R}}$+$\mathrm{ER}^{\mathrm{M}}$-algorithm will be illustrated for a nanostructure for which the displacement field u has been obtained by finite element modeling (FEM) of linear elasticity theory (LET) [44–49]. This displacement field and the shape of the nanostructure were extracted and used for the generation of the input data of the reconstructions. We focus on a periodic array of Si-(001)-nanowires like the one studied experimentally by Eberlein et al. [50,51]. Their samples have been fabricated by etching trenches in a silicon substrate (black domain in Fig. 2(a)). These trenches have been filled with amorphous silicon-oxide SiO_2 (gray domain in Fig. 2(a)). Different thermal expansion coefficients of the crystalline and amorphous region result in non-vanishing strain in the nanostructure after cooling down to room temperature.

For our simulations of the Si-nanowire system, the commercial FEM software "COMSOL Multiphysics" was used to calculate the desired displacement field u. Translational symmetry along the wires allows performing the simulation in a planar cut perpendicular to the direction of the wires. Thus, the system can be treated in two dimensions. Due to the periodic arrangement of the wires, simulations are restricted to a single block of the periodic object.

The geometry and dimensions of the system are as follows: the lateral periodicity is 200nm. The substrate has been etched to a depth of 237nm in vertical direction and filled with amorphous silicon oxide to a height of approximately 258nm which results in a cap layer of 21nm thickness. A 1000nm thick substrate domain below the bottom of the nanowire was included.

In our numerical simulations in Sec. 2, we increase the sample's strain by linear rescaling of the displacement field u. The strain distribution is characterized by its maximum strain $\varepsilon_\mathrm{M} = \max(\partial_z u_z)$ in the crystalline part on the wire's central axis. The resulting phase field of the effective electron density for the values $\varepsilon_\mathrm{M} = \{0.10\%, 0.30\%, 0.60\%\}$ is depicted in Figs. 2(b)-2(d). In addition, Figs. 2(e)-2(g) gives an impression of the scattering signal Γ_q for $\varepsilon_\mathrm{M} = \{0.10\%, 0.20\%, 0.28\%\}$.

#192722 - $15.00 USD Received 21 Jun 2013; revised 30 Aug 2013; accepted 2 Sep 2013; published 5 Nov 2013

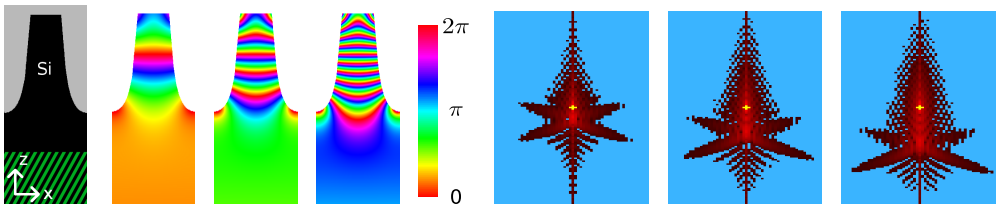

(a) Si-NW geometry (b) $\varepsilon_M = 0.1\%$ (c) $\varepsilon_M = 0.3\%$ (d) $\varepsilon_M = 0.6\%$ (e) $\varepsilon_M = 0.10\%$ (f) $\varepsilon_M = 0.20\%$ (g) $\varepsilon_M = 0.28\%$

Fig. 2. Illustration of the physical system used for our investigation of the $\mathrm{HIO}^{\mathrm{M}}_{\mathrm{O_R}}$+$\mathrm{ER}^{\mathrm{M}}$-algorithm. Figure (a) shows the geometry and composition of the upper region of a periodic unit of the periodic Si-nanowire system. The hatched domain will become important in next sections. Figures (b)-(d) depict the phase field $Q_B \cdot u(x)$ of effective electron density $\rho_{\mathrm{eff}}(x)$ for this system for different values of the maximum strain ε_M on the wires' symmetry axis in the crystalline domain, if the Bragg peak $Q_B = [004]$ is investigated. Figures (e)-(g) show the scattering signal in presence of the low signal cutoff Γ_N (see Sec. 1.4). Only the central region of the scattering signal around the Bragg peak Q_B is shown (Q_B is located at the yellow dot). Data points below the noise level Γ_N are masked in dark cyan.

1.3. *Measures for success in numerical simulations*

The results ρ_{eff} of the iterative reconstructions after (i) iterations of the $\mathrm{HIO}^{\mathrm{M}}_{\mathrm{O_R}}$+$\mathrm{ER}^{\mathrm{M}}$-algorithm are compared to the perfect solution $\rho_{\mathrm{eff}}(x)$ by evaluating

$$\varphi^{(i)} = \arccos\left[\left|\left\langle \rho^{(i)}_{\mathrm{eff}}\,;\rho_{\mathrm{eff}}\right\rangle\right| \Big/ \sqrt{\left\langle \rho^{(i)}_{\mathrm{eff}}\,;\rho^{(i)}_{\mathrm{eff}}\right\rangle\left\langle \rho_{\mathrm{eff}}\,;\rho_{\mathrm{eff}}\right\rangle}\right] . \tag{13}$$

This measure eliminates the undefined global phase in the reconstructed effective electron density (see Sec. A in the appendix).

The iterative reconstruction procedure has been terminated if either a maximum number of iterations was reached or if the change of ρ_{eff} from iteration to iteration dropped below a certain value. This change has been monitored by the angle

$$\chi^{(i)} = \arccos\left[\left|\left\langle \rho^{(i-1)}_{\mathrm{eff}}\,;\rho^{(i)}_{\mathrm{eff}}\right\rangle\right| \Big/ \sqrt{\left\langle \rho^{(i-1)}_{\mathrm{eff}}\,;\rho^{(i-1)}_{\mathrm{eff}}\right\rangle\left\langle \rho^{(i)}_{\mathrm{eff}}\,;\rho^{(i)}_{\mathrm{eff}}\right\rangle}\right] . \tag{14}$$

In [1], Köhl et al. provided a more detailed discussion of Eqs. (13) and (14).

1.4. *Artifacts in reciprocal space*

Our simulated input data for the reciprocal space amplitudes Γ_q exhibits a signal to noise ratio which is limited only by finite digit precision. In contrast to that, the signal to noise ratio of the experimental scattering data used by Minkevich et al. in [24, 25] had signal to noise ratio of approximately 100 (in the diffuse cloud, excluding the central Bragg peak). As a consequence, most data points in reciprocal space are corrupted by noise and additional diffuse scattering, e.g., by optical elements, Be windows of vacuum flight tubes, etc. . Thus, their true value is inaccessible by current experimental measurements: for those data points we should only assume that they are bound by the noise level Γ_N from above, i.e., $\Gamma_q \leq \Gamma_N$. As no beamstop is required in case of imaging strained nanocrystals at $Q_B \neq \vec{0}$ (in contrast to performing diffractive imaging measurements in forward direction $Q_B = \vec{0}$ [52]), this upper bound Γ_N is well defined and experimentally accessible.

#192722 - $15.00 USD Received 21 Jun 2013; revised 30 Aug 2013; accepted 2 Sep 2013; published 5 Nov 2013

Table 1. Definition of κ_q for five models (A)-(E) which are investigated for treating data points below a given low cutoff Γ_{N}.

Condition — Model	(A)	(B)	(C)	(D)	(E)
if $\Gamma_q > \Gamma_{\mathrm{N}}$	Γ_q	Γ_q	Γ_q	Γ_q	Γ_q
if $(\Gamma_q \leq \Gamma_{\mathrm{N}}) \wedge (\lvert\mathfrak{f}_q^{(i)}\rvert \leq \Gamma_{\mathrm{N}})$	0	$\lvert\mathfrak{f}_q^{(i)}\rvert$	$\lvert\mathfrak{f}_q^{(i)}\rvert$	$\lvert\mathfrak{f}_q^{(i)}\rvert$	$c_{\mathrm{D}}\lvert\mathfrak{f}_q^{(i)}\rvert$
if $(\Gamma_q \leq \Gamma_{\mathrm{N}}) \wedge (\lvert\mathfrak{f}_q^{(i)}\rvert > \Gamma_{\mathrm{N}})$	0	0	$\mathrm{r}_{0;\Gamma_{\mathrm{N}}}$	Γ_{N}	Γ_{N}

In this manuscript, we compare five strategies for treating data points $\Gamma_q \leq \Gamma_{\mathrm{N}}$. We hope that our investigation will contribute to establishing CXDI of inhomogeneously strained nanostructures as a robust technique of experimental value. The investigation of other artifacts (like the "inconsistent" Bragg peak in experimental data, photon noise in the signal $\mathbf{I}_q$ [7], smearing of $\mathbf{I}_q$ by instrumental effects and corrections from higher order scattering beyond kinematic approximation) goes beyond the scope of this manuscript.

In all five approaches the definition of $\mathbf{P}_\Gamma$ as given in Eq. (6) is modified to

$$\mathbf{P}_\Gamma\, \mathfrak{f}^{(i)}(q) = \kappa_q\, \mathrm{e}^{\mathrm{i}\, \arg\left(\mathfrak{f}^{(i)}(q)\right)}\,. \tag{15}$$

The individual approaches differ in the definition of κ_q and are defined in Table 1.

The first approach (A) incorporates the noisy region as the weak signal limit, i.e., approximating all amplitudes below the lower cutoff Γ_{N} as zero. However, small inconsistencies between direct space support Ω and Fourier space amplitudes κ_q are inevitable in this approach. Therefore, our second, third and fourth approach allow the reciprocal space amplitude at every q-point to evolve freely until it exceeds the given cutoff Γ_{N}. The approaches differ in the behavior if the cutoff is exceeded during the iterative procedure: In the second approach (B), the respective amplitude is reset to zero. In the third approach (C), it is reset to a random value in the interval $[0,\Gamma_{\mathrm{N}}]$ (uniform distribution). The fourth approach (D) resets the amplitude only to its upper bound Γ_{N}. Finally, the fifth approach (E) contains a small damping $c_{\mathrm{D}} \lesssim 1$ in regions below Γ_{N}. This way, we regularize the corrupted region such that high frequency contributions to the direct space effective electron density $\rho_{\mathrm{eff}}(x)$ are suppressed. Note, that the last approach (E) reduces to the fourth approach (D) in the limit $c_{\mathrm{D}} \to 1$.

2. Results

In this section, we present the results of our numerical investigation. We focus on the success rate $s \in [0\%, 100\%]$ of fully automated reconstructions (no user interaction like tuning of parameters during reconstruction). The success rate is a statistical quantity for all cases we consider, because random numbers influence the reconstruction at two stages: first, the initial guess itself is based on random phases for the given amplitudes in reciprocal space. Therefore, the success rate s is a statistical quantity even for the traditional HIO+ER-algorithm. Second, for those reconstructions that exploit randomized overrelaxation ($\nu > 0$), the iterative approximation to the solution varies from one trial to another even for the same initial guess. Therefore, we estimate the success rate s by evaluating a set of $\mathrm{N}_{\mathrm{Real}} = 100$ trials. Every trial has its own random initial guess and its own random overrelaxation parameters λ_Γ. For a robust, automated reconstruction, this success rate should reach values close to 100% within a practical number of iterations N_{Iter}.

The success rate s may depend on the strain ε_{M}, the number of iterations (i) which has been performed and our choice of the angle φ_{Max} which is used to distinguish successful reconstructions from failed reconstructions based on Eq. (13). We will investigate its behavior by

#192722 - $15.00 USD Received 21 Jun 2013; revised 30 Aug 2013; accepted 2 Sep 2013; published 5 Nov 2013

two-dimensional cuts through this three dimensional parameter space and use a unified color-coding to encode the success rate s.

The rectangular discretization grid contained 232x798 pixels ($N_{Tot} = 185136$). A single pixel corresponds to a distance of 0.862nm in x-direction and 1.575nm in z-direction. The substrate was truncated in such a way that an oversampling σ of 3.6326 has been achieved. The parameters of the reconstructions were chosen as $N_{ER} = 10$, $N_{HIO} = 130$, $\beta = 0.8$, $c_D = 0.99$ and either $\nu = 0$ ("without randomized overrelaxation") or $\nu = 0.5$ ("with randomized overrelaxation"). The reconstruction procedure was terminated, if either $N_{Iter} = 500$ iterations have been performed or the change of the iterative approximation from the current to the previous approximation $\chi^{(i)}$ as defined in Eq. (14) dropped below 10^{-6} rad.

2.1. *Full reciprocal space information within the framework defined by Eqs.* (2) *and* (3)

We first focus on the case $\Gamma_N = 0$ in Fig. 3. Figures 3(a)-3(d) are devoted to the classical HIO+ER-algorithm ($\nu = 0$ and no constraints on ζ). The range ε_M from 0.02% to 0.40% was covered in steps $\delta\varepsilon_M = 0.02\%$. For a maximum strain up to $\varepsilon_M = 0.10\%$, all trials converged to the solution ρ_{eff} within very few iterations (see Fig. 3(a) as well as Figs. 2(b) and 2(e)). For $\varepsilon_M = 0.12\%$ the success probability dropped down to $s = 38\%$, for $\varepsilon_M = 0.16\%$ to $s = 15\%$ and for any $\varepsilon_M > 0.20\%$ (see Fig. 2(f)), success probability was essentially $s = 0\%$. In the range $\varepsilon_M = 0.12\%$ to $\varepsilon_M = 0.20\%$, sometimes stagnation close to the solution ρ_{eff} can be observed (see Figs. 3(b) and 3(c)). However, in most cases stagnation is observed on a level φ far from the true solution ($\varphi > 20°$). Figures 3(c) and 3(d) demonstrate that once the classical HIO+ER-algorithm is stuck in a level of stagnation, the mean number of iterations that the iterative procedure remains there is very high, even if this level is far from the solution ρ_{eff}.

Next, we benchmark the impact of randomized overrelaxation on the traditional HIO+ER-algorithm (i.e., $\nu > 0$) in Figs. 3(e)-3(h). In the range $\varepsilon_M \leq 0.10\%$, no negative penalty of randomized overrelaxation has been discovered (see Fig. 3(e)). Within the range $\varepsilon_M = 0.12\%$ to $\varepsilon_M = 0.28\%$ (see Fig. 2(g)), the HIO_{O_R}+ER-algorithm is clearly superior to the classical HIO+ER-algorithm (see Fig. 3(e)). Successful reconstructions are possible independent of the random initial guess with a success probability s close to 100% within $i = 500$ iterations. However, the number of iterations which is required to achieve a success rate close to 100% is increasing with increasing strain (see Fig. 3(e)). Figures 3(f)-3(h) investigate this observation in more detail and are to be compared to Figs. 3(c)-3(d) for the traditional HIO+ER-algorithm. In contrast to the traditional HIO+ER-algorithm, the iterative reconstruction procedure with randomized overrelaxation manages to escape from levels of stagnation up to $\varepsilon_M \geq 0.28\%$ within a reasonable number of iterations ($i < 500$). This behavior can be observed particularly well for $\varepsilon_M \geq 0.26\%$ in Fig. 3(h). Finally, for $\varepsilon_M \geq 0.30\%$ (see Fig. 2(c)), robust automatic reconstructions are not possible even with randomized overrelaxation within $i = 500$ iterations.

The rest of Fig. 3 is dedicated to the investigation of the impact of bounds on the local scattering magnitude: Whereas Figs. 3(i)-3(l) illustrate the behavior of the success rate s for the traditional HIO+ER-algorithm extended for bounds on the local scattering magnitude ζ without randomized overrelaxation, Figs. 3(m)-3(p) demonstrate the benefits from the combination of randomized overrelaxation and our constraints on the local scattering magnitude.

In the reconstructions underlying Figs. 3(i), 3(j) and 3(m), $\zeta(x)$ was constrained by $M_{L,} = M_{H,} = 1.0$ in the full domain Ω. Most importantly, we observe, that such strict lower and upper bounds on $\zeta(x)$ tremendously enhance the range of applicability: Without randomized overrelaxation, almost stagnation free reconstructions proved to be possible up to approximately $\varepsilon_M \lesssim 0.56\%$ (see Fig. 2(d)) — in contrast to $\varepsilon_M \lesssim 0.10\%$ without such bounds (see Fig. 3(a)). Moreover, even up to $\varepsilon_M = 1.00\%$, some random initial trails have converged to the solution ρ_{eff} (compared to $\varepsilon_M \lesssim 0.20\%$ for traditional HIO+ER-algorithm). However, if a random initial

#192722 - $15.00 USD Received 21 Jun 2013; revised 30 Aug 2013; accepted 2 Sep 2013; published 5 Nov 2013

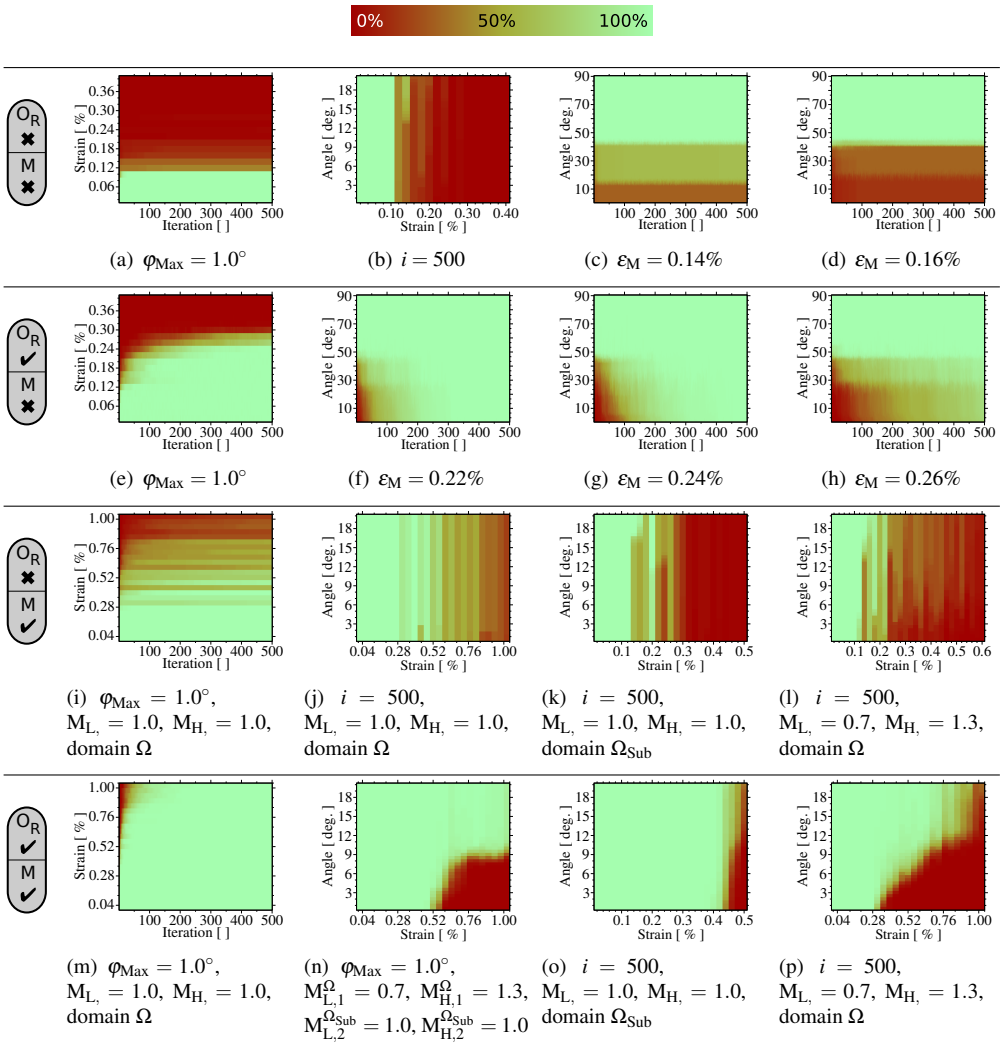

(a) $\varphi_{\mathrm{Max}} = 1.0^\circ$ (b) $i = 500$ (c) $\varepsilon_{\mathrm{M}} = 0.14\%$ (d) $\varepsilon_{\mathrm{M}} = 0.16\%$

(e) $\varphi_{\mathrm{Max}} = 1.0^\circ$ (f) $\varepsilon_{\mathrm{M}} = 0.22\%$ (g) $\varepsilon_{\mathrm{M}} = 0.24\%$ (h) $\varepsilon_{\mathrm{M}} = 0.26\%$

(i) $\varphi_{\mathrm{Max}} = 1.0^\circ$, $\mathrm{M}_{\mathrm{L,}} = 1.0$, $\mathrm{M}_{\mathrm{H,}} = 1.0$, domain Ω

(j) $i = 500$, $\mathrm{M}_{\mathrm{L,}} = 1.0$, $\mathrm{M}_{\mathrm{H,}} = 1.0$, domain Ω

(k) $i = 500$, $\mathrm{M}_{\mathrm{L,}} = 1.0$, $\mathrm{M}_{\mathrm{H,}} = 1.0$, domain Ω_{Sub}

(l) $i = 500$, $\mathrm{M}_{\mathrm{L,}} = 0.7$, $\mathrm{M}_{\mathrm{H,}} = 1.3$, domain Ω

(m) $\varphi_{\mathrm{Max}} = 1.0^\circ$, $\mathrm{M}_{\mathrm{L,}} = 1.0$, $\mathrm{M}_{\mathrm{H,}} = 1.0$, domain Ω

(n) $\varphi_{\mathrm{Max}} = 1.0^\circ$, $\mathrm{M}^{\Omega}_{\mathrm{L,1}} = 0.7$, $\mathrm{M}^{\Omega}_{\mathrm{H,1}} = 1.3$, $\mathrm{M}^{\Omega_{\mathrm{Sub}}}_{\mathrm{L,2}} = 1.0$, $\mathrm{M}^{\Omega_{\mathrm{Sub}}}_{\mathrm{H,2}} = 1.0$

(o) $i = 500$, $\mathrm{M}_{\mathrm{L,}} = 1.0$, $\mathrm{M}_{\mathrm{H,}} = 1.0$, domain Ω_{Sub}

(p) $i = 500$, $\mathrm{M}_{\mathrm{L,}} = 0.7$, $\mathrm{M}_{\mathrm{H,}} = 1.3$, domain Ω

Fig. 3. Behavior of the $\mathrm{HIO}^{\mathrm{M}}_{\mathrm{O_R}}$+$\mathrm{ER}^{\mathrm{M}}$-algorithm (including its limiting cases without randomization and/or without constraints on the local scattering magnitude, see grey boxes with black border at the beginning of each row of four subfigures) for ideal data: Depicted are two-dimensional cuts of the success rate s through the three dimensional parameter space for either fixed strain ε_{M}, number of iterations i or angle φ_{Max}. We count all random initial trails as success for which the angle $\varphi^{(i)}$ (defined in Eq. (13)) to the reference solution ρ_{eff} is below φ_{Max} in iteration (i) for that particular value of strain ε_{M}. The domain Ω_{Sub} corresponds to the hatched domain in Fig. 2(a).

trial stagnated, it typically stagnated on a level $\varphi \geq 20^\circ$, i.e., far from the solution.

Therefore, stagnation like for classical HIO is persistent even with the additional *a priori* knowledge, but without randomized overrelaxation.

At $\varepsilon_{\mathrm{M}} = 1.0\%$ we stopped our investigation because the number of pixels in discrete numerical grid representing the fastest 2π-oscillation in the effective electron density ρ_{eff} dropped to approximately eight pixels.

If randomized overrelaxation is switch on, no stagnation remains up to $\varepsilon_{\mathrm{M}} \geq 1.00\%$ (see Fig.

#192722 - $15.00 USD Received 21 Jun 2013; revised 30 Aug 2013; accepted 2 Sep 2013; published 5 Nov 2013

Table 2. Characteristics of reciprocal space input data Γ_q in case of low signal cutoff Γ_N.

ε_M	σ_{eff}	# points $> \Gamma_N$	$\frac{\#\text{ points} > \Gamma_N}{N_{\text{Tot}}}$	$\frac{\left\|\Gamma_q < \Gamma_N\right\|_1}{\left\|\Gamma_q\right\|_1}$	$\frac{\left\|\Gamma_q < \Gamma_N\right\|_2}{\left\|\Gamma_q\right\|_2}$
0.10%	0.0304	1548	0.84%	64.6%	0.433%
0.20%	0.0392	2000	1.08%	59.7%	0.401%
0.28%	0.0442	2255	1.22%	56.3%	0.396%

3(m)): reconstructions typically reach a distance of $\varphi = 1.0^\circ$ to the solution ρ_{eff} for iterations $i \ll 500$.

If we apply $M_{L,} = M_{H,} = 1.0$ only in the substrate region Ω_{Sub} (thickness in z-direction equal to 80 pixel, hatched domain in Fig. 2(a)), we can observe the behavior depicted in Fig. 3(k) for $\nu = 0$ (no overrelaxation) and in Fig. 3(o) for $\nu = 0.5$ (with overrelaxation). Again, the benefits of lower and upper bounds on the magnitude in direct space and randomized overrelaxation are clearly visible.

Moreover, we can relax the bounds $M_{L,}$ and $M_{H,}$. The results for $M_{L,} = 0.7$ and $M_{H,} = 1.3$ are depicted in Figs. 3(l) and 3(p). Without randomized overrelaxation (see Fig. 3(l)), stagnation is still very strong, but at least some random initial trials converged to a level close to the true solution. Interestingly, even randomized overrelaxation does not eliminate stagnation for such bounds (see Fig. 3(p)): nevertheless, the behavior becomes independent of the random initial trail and manages to come close to the true solution. The latter is not true for $\varepsilon_M \geq 0.30\%$ without bounds on the local scattering magnitude. Up to $\varepsilon_M = 0.28\%$ — the limit for successful reconstructions without bounds for the local scattering magnitude — no negative penalty is observed.

2.2. *Low signal cutoff in reciprocal space*

Next, we investigate the capabilities of the $\text{HIO}^{M}_{O_R}$+ER^{M}-algorithm for finite low cutoff $\Gamma_N > 0$ (see Sec. 1.4). To be specific, we define for every value of strain ε_M the low cutoff Γ_N as $\Gamma_N = \mu \ \max_q(\Gamma_q)$ where $\mu = 0.005$. If we exclude the Bragg peak, this value for μ corresponds approximately to the experimental value for the signal to noise ratio which we mentioned in the beginning of the section 1.4. Figures 2(e)-2(g) show which part of the scattering signal for the particular values of strain $\varepsilon_M = 0.10\%$, $\varepsilon_M = 0.20\%$ and $\varepsilon_M = 0.28\%$ exceeds this noise level Γ_N. We define the effective oversampling ratio σ_{eff} as the ratio of the number of data points exceeding the noise level Γ_N divided by the number of data points inside the direct space support. It is listed in Table 2 together with the number and percentage of data points in the scattering signal exceeding the cutoff Γ_N. Moreover, this table contains the fraction of the $\mathscr{L}_1$- and $\mathscr{L}_2$-norm which is accumulated in the scattering signal below the cutoff. The effective oversampling ratio is in the range of $\sigma_{\text{eff}} = 0.03$ to $\sigma_{\text{eff}} = 0.05$ for the cases we present here. The "residual" approximately 99% of data points need to be regularized in such a way that the small fraction of data points exceeding Γ_N is sufficient for a successful reconstruction. Of course, the precise values in Table 2 depend on the spacing of the discretization grid in direct space (or equivalent: the extension of the domain in reciprocal space): A grid with larger interpixel spacing in direct space will suffer from aliasing artifacts. On the contrary, a finer grid will reduce the effective oversampling even further and, therefore, relies even more on an efficient approach for low signal data points. However, the optimal choice of the direct space pixel grid goes beyond the scope of this manuscript.

For the investigation of our models (A) to (E) as defined in Table 1, we need to eliminate the amplitude information Γ_q from the initial guess (8) if $\Gamma_q \leq \Gamma_N$. Therefore, we enforce $\Gamma_q = 0$ for $\Gamma_q \leq \Gamma_N$ in the initial guess. Moreover, we now need to take instabilities into account which

#192722 - $15.00 USD Received 21 Jun 2013; revised 30 Aug 2013; accepted 2 Sep 2013; published 5 Nov 2013

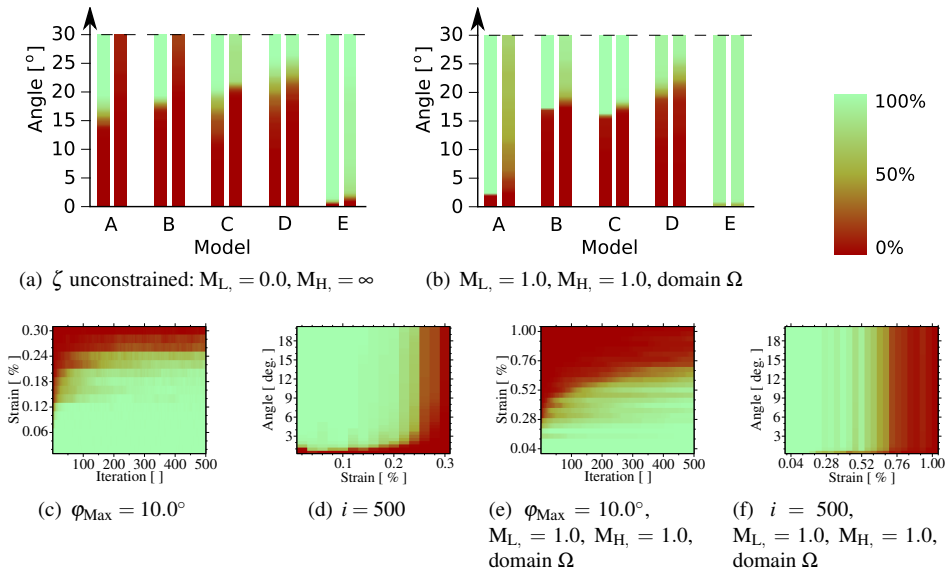

(a) ζ unconstrained: $M_{L,} = 0.0$, $M_{H,} = \infty$ (b) $M_{L,} = 1.0$, $M_{H,} = 1.0$, domain Ω

(c) $\varphi_{Max} = 10.0°$ (d) $i = 500$ (e) $\varphi_{Max} = 10.0°$, $M_{L,} = 1.0$, $M_{H,} = 1.0$, domain Ω (f) $i = 500$, $M_{L,} = 1.0$, $M_{H,} = 1.0$, domain Ω

Fig. 4. Characteristics of the $HIO^{M}_{O_R}$+ER^{M}-algorithm in presence of a low cutoff Γ_N. Figures (a) and (b) compare the success rate s of the models defined in Sec. 1.4 for fixed strain $\varepsilon_M = \{0.20\%, 0.28\%\}$ after $i = 500$ iterations. Figures (c)-(f) contain two-dimensional plots of the success rate s for model (E) (analogue to Fig. 3). For Figs. (a), (c) and (d), no constraints on ζ have been applied. Figures (b), (e) and (f) illustrate the improvement if bounds on the local scattering magnitude are taken into account. Note the different range of the strain axes.

have not occurred in our reconstructions for ideal data: For every reconstruction trial (each of the $N_{Real} = 100$ trials with new random initial phases) we extract two numbers: First, we extract the smallest distance $\varphi^{(i)}$ which was achieved at any iteration $i \leq 500$ (left bars in Figs. 4(a) and 4(b)). Second, we extract the distance $\varphi^{(500)}$, i.e., the distance to the solution ρ_{eff} after $i = 500$ iterations (right bars in Figs. 4(a) and 4(b)). Thus, the left bars in Figs. 4(a) and 4(b) are important if we find some robust criterion for selecting the best approximation $\rho^{(i)}_{eff}$ from the set $\{\rho^{(i)}_{eff}\}$, $i \in [0, 500]$, whereas the right bars are important as long as such a criterion is not available. Figure 4(a) compares the models (A) to (E) if no bounds on local scattering magnitude are applied. For the data depicted in Fig. 4(b) strict bounds on the local scattering amplitude ($M_{L,} = M_{H,} = 1.0$ in entire domain Ω) have been exploited. We observe that model (A) (i.e., setting the low signal amplitudes simply to zero) results in very unstable behavior. Model (B) is unstable without constraints on the local scattering magnitude, but partially regularized in presence of such constraints. Nevertheless, none of the models (B) to (D) succeeds in achieving a small angle $\varphi \leq 10.0°$ to the solution ρ_{eff}. The small damping underlying model (E) provides the by far best results.

For model (E), the success rate s is depicted as a function of strain ε_M vs. iteration i and as a function of angle φ_{Max} vs. strain ε_M in Figs. 4(c)-4(f), where the reciprocal space data described by the non-zero cutoff in Table 2 has been used. In both cases, the success rate is almost independent of the choice φ_{Max} for $\varphi_{Max} \in [3.0°, 20.0°]$.

In comparison to reconstructions without cutoff in reciprocal space (i.e., $\Gamma_N = 0$), the maximum strain ε_M which could be reconstructed in the framework of model (E) (with low cutoff $\mu = 0.005$ resulting in effective oversampling ratios $\sigma_{eff} \approx 0.03$ to $\sigma_{eff} \approx 0.05$) dropped

#192722 - $15.00 USD Received 21 Jun 2013; revised 30 Aug 2013; accepted 2 Sep 2013; published 5 Nov 2013

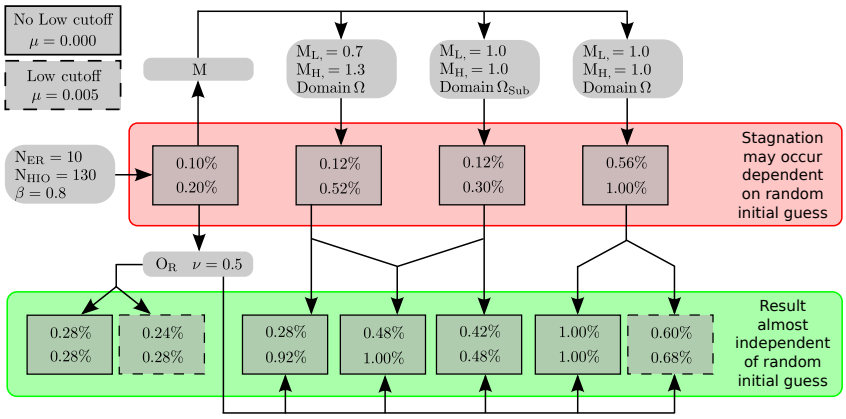

Fig. 5. Summary of our numerical investigation: Starting from standard HIO+ER, the improvements which are achieved by randomized overrelaxation and the additional constraints M on the local scattering magnitude ζ are simplified to two values. The upper value in each rectangular box is the maximum strain ε_M for which an almost perfect solution could be reconstructed within $i = 500$ iterations and for almost all random initial trails. The lower value is the maximum strain ε_M for which the reconstruction of the effective electron density $\rho_{\text{eff}}^{(500)}$ was successful if the requirement for success is relaxed: Any strain ε_M for which at least some non-negligible fraction of initial guesses managed to achieve a result close to the solution ρ_{eff} ($\varphi_{\text{Max}} \lesssim 10.0°$) is classified as suitable for the respective approach and constraints.

from $\varepsilon_M \approx 0.28\%$ to $\varepsilon_M \approx 0.24\%$ without constraints on the local scattering magnitude ζ. If strict bounds on ζ in the entire domain Ω are enforced in the framework of the $\text{HIO}_{\text{O}_R}^{\text{M}}$+$\text{ER}^{\text{M}}$-algorithm, the maximum strain ε_M which could be reconstructed drops from $\varepsilon_M \geq 1.0\%$ to $\varepsilon_M \approx 0.68\%$. This corresponds approximately to the phase field illustrated in Fig. 2(d). Keep in mind that many other important artifacts in experimental data need to be taken care of which we did not discuss in this manuscript, but will be subject of future research.

3. Conclusion

By combining randomized overrelaxation and easily accessible, but widely applicable additional *a priori* knowledge of the local scattering magnitude to the $\text{HIO}_{\text{O}_R}^{\text{M}}$+$\text{ER}^{\text{M}}$-algorithm, we succeeded in achieving success rates of the reconstruction procedure close to 100% for many strain values which are very likely to fail without our modifications. Thus, the $\text{HIO}_{\text{O}_R}^{\text{M}}$+$\text{ER}^{\text{M}}$-algorithm provides significant improvements over the traditional HIO+ER-algorithm: reconstructions of highly strained objects with barely no stagnation became possible. Moreover, the $\text{HIO}_{\text{O}_R}^{\text{M}}$+$\text{ER}^{\text{M}}$-algorithm inherits the good computational scaling of the traditional HIO+ER-algorithm and is easy to implement. Thus, current limitations of CXDI data analysis are shifted to significantly higher values of strain.

Given the greatly improved performance of the $\text{HIO}_{\text{O}_R}^{\text{M}}$+$\text{ER}^{\text{M}}$-algorithm for ideal data, we systematically investigated the consequences of one major experimental artifact on the reconstruction process: We compared different models for treating data points in reciprocal space with such a low intensity that their true value cannot be obtained in current experiments. Most data points in reciprocal space need to be classified in that category resulting in typical effective oversampling ratios $\sigma_{\text{eff}} \ll 1$ (see Table 2). In our comparison the combination of a small damping and limiting the reciprocal space amplitude by noise level Γ_N from above turned out to be the most efficient model by far.

#192722 - $15.00 USD Received 21 Jun 2013; revised 30 Aug 2013; accepted 2 Sep 2013; published 5 Nov 2013

Figure 5 gives a graphical summary of our numerical investigation: Starting from standard HIO+ER, the improvements which are achieved by including randomized overrelaxation and the additional constraints $\mathbf{M}_\mathrm{M}$ separately or combined can be found. From this figure, our three major results can be read off easily: First, the additional bounds on the local scattering magnitude — incorporated by the mapping $\mathbf{M}_\mathrm{M}$ — enhance the range of applicability up to a factor of five, but the result still depends on the random initial guess. Second, randomized overrelaxation manages to eliminate the sensitivity to the random initial guess to a large degree — with and without the constraints $\mathbf{M}_\mathrm{M}$. Third, randomized overrelaxation manages to increase the range of applicability further (without any additional *a priori* knowledge) in all cases we presented. Therefore, we are confident that the combination of randomized overrelaxation $\mathbf{Q}_{\Gamma;\lambda_\Gamma}$ and the local scattering magnitude constraints $\mathbf{M}_\mathrm{M}$ enhances current possibilities to reconstruct the atomic displacement field from CXDI measurements.

As an outlook we point out that the impact of further experimental artifacts and limitations on the reconstruction needs to be studied in a systematic way for a complete picture. This will be a topic of future research activities. Moreover, the magnitude constraints (9) which we presented here can also be further generalized: One possibility is to add couplings of the averages of different domains and/or a global average in addition. This way, further *a priori* known correlations of the effective electron density are added to the reconstruction process.

A. Uniqueness and discretization

The solution of the model Eqs. (2) and (3) is only unique up to some inherent, unavoidable ambiguities resulting from the mathematical properties of the Fourier transform: Shifting the object in position space only results in a plane wave modulation in reciprocal space. Hence, it produces the same intensity distribution $\mathbf{I}_{Q_\mathrm{B}}(q)$. These ambiguities are removed by fixing the position of the shape Ω in position space. If the shape Ω of the nanocrystal is inversion symmetric, an additional twofold ambiguity shows up: Both, $\rho_\mathrm{eff}(x)$ and $\rho^*_\mathrm{eff}(-x)$ fulfill all constraints enforced by the input data and, therefore, constitute two distinct solutions unless $\rho_\mathrm{eff}(x) \propto \rho^*_\mathrm{eff}(-x)$. We avoid this ambiguity by investigating a nanostructure with non inversion symmetric shape. The only remaining ambiguity indicated by the mathematical properties of the Fourier transform is a physically irrelevant global phase shift which is not constrained in our reconstruction. Instead, the mathematical measure which we employ for judging upon the success of a reconstruction is insensitive to this ambiguity (see Sec. 1.3).

For the numerical treatment of Eqs. (2) and (3), position space and reciprocal space are sampled on an rectangular equidistant grid and the continuous Fourier transform is approximated by its discretized version, i.e., the DFT [53]. The spacing δx_m and δq_m of the grid in direction m is connected to the domain boundaries ranging from $(-X_m, X_m)$ and $(-\Omega_m, \Omega_m)$ via $\delta x_m = \frac{2X_m}{N_m}$, $\delta q_m = \frac{2\Omega_m}{N_m}$ and $N_m = \frac{2\pi}{\delta q_m\, \delta x_m}$. This implies that by fixing Ω_m and δq_m, we implicitly choose values for N_m, δx_m and X_m. In theory, knowledge of the amplitudes Γ_q and the shape $\Omega(x)$ is sufficient, if the shape Ω is finite, the dimensionality of the structure is at least equal to two and the distance δq of the measured points in reciprocal space is small enough to guarantee a sufficient oversampling ratio σ on the grid ($\sigma \geq 2$ is a lower bound) [1, 26, 54–56].

Acknowledgments

M. K. would like to acknowledge productive and useful discussions on structure and clarity of this manuscript with Alexey Ershov and Marthe Kaufholz. A. A. M. is very grateful to Marc Gailhanou and Olivier Thomas who initiated the research with such kind of nanostructures.

#192722 - $15.00 USD Received 21 Jun 2013; revised 30 Aug 2013; accepted 2 Sep 2013; published 5 Nov 2013